Chemical and Biochemical Engineering Faculty Research & Creative Works

Linda and Bipin Doshi Department of Chemical and Biochemical Engineering

15 Feb 2019

The Effect of Calcination Rate on the Structure of Mesoporous Bioactive Glasses

Saidur Rahman

Andrew Mendonca

Adel Alhalawani

Deanna Polintan

et. al. For a complete list of authors, see https://scholarsmine.mst.edu/che_bioeng_facwork/1082

Recommended Citation

ORIGINAL PAPER: FUNDAMENTALS OF SOL-GEL AND HYBRID MATERIALS PROCESSING

The effect of calcination rate on the structure of mesoporous bioactive glasses

Saidur Rahman[1,2] · Andrew Mendonca[2,3] · Adel Alhalawani[1,2] · Deanna Polintan[2,3] · Owen M. Clarkin[4] · Mark R. Towler[1,2]

Abstract

Mesoporous bioactive glasses (MBGs) are designed to have high specific surface area. They are formulated by a sol–gel process to formulate the glass followed by calcination. This study evaluates how calcination heating rate influences the porous architecture, and thereby the specific surface area, of MBGs. MBGs of molar ratio 80:15:5 for SiO_2:CaO:P_2O_5 were calcined using both low (1 °C/min) and high (20 °C/min) heating rates, termed as L-MBG and H-MBG, respectively. The results obtained from small-angle X-ray diffraction (SAXRD) confirm that the MBGs possess 2D hexagonal (P6mm) spacing groups and wide-angle XRD confirms the amorphicity of both MBGs. Energy-dispersive X-ray spectroscopy and X-ray photoelectron spectroscopy confirm that both batches of MBGs have similar chemical composition. Fourier transform infrared spectroscopy identifies the same functional groups present in both batches. However, transmission electron microscopy indicates that H-MBG samples exhibited discontinuities in their ordered channel structure, confirmed by the lower SAXRD peak intensity of H-MBG compared to L-MBG. These discontinuities led to a reduced surface area. L-MBG exhibits more than quadruple the surface area and double the pore volume (373.87 m^2/g and 0.27 cm^3/g) of H-MBG (85.91 m^2/g and 0.13 cm^3/g), measured through Brunauer, Emmett, and Teller nitrogen adsorption analysis. This higher surface area resulted in a significant ($p < 0.05$) increase in the quantity of ion release from the L-MBGs compared to the H-MBGs. It is concluded that the application of a low heating rate during calcination, of the order of 1 °C/min, is more likely to result in ordered mesoporous bioactive glasses with high surface area and pore volume than MBG samples processed at a higher heating rate.

✉ Adel Alhalawani
  adel.alhalawani@ryerson.ca

1 Department of Mechanical and Industrial Engineering, Ryerson University, Toronto, Ontario M5B 2K3, Canada
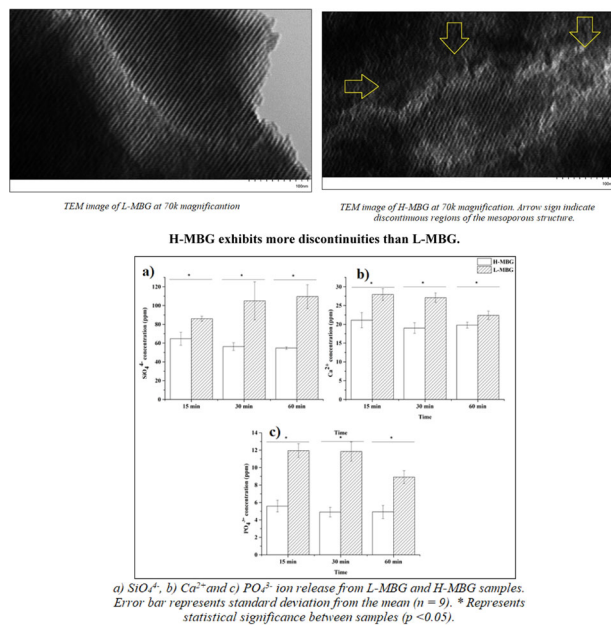
2 Li Ka Shing Knowledge Institute, St. Michael's Hospital,

Toronto, Ontario M5B 1W8, Canada

3 Department of Biomedical Engineering, Ryerson University, Toronto, Ontario M5B 2K3, Canada

4 School of Mechanical & Manufacturing Engineering, Dublin City University, Dublin, Ireland

Graphical Abstract

TEM image of L-MBG at 70k magnification

TEM image of H-MBG at 70k magnification. Arrow sign indicate discontinuous regions of the mesoporous structure.

H-MBG exhibits more discontinuities than L-MBG.

*a) SiO_4^{4-}, b) Ca^{2+} and c) PO_4^{3-} ion release from L-MBG and H-MBG samples. Error bar represents standard deviation from the mean (n = 9). * Represents statistical significance between samples (p < 0.05).*

Highlights

- Calcination rate (low or high) has no effect on the chemical composition of mesoporous bioactive glasses (MBGs).
- Calcination rate influences the physical structure of MBGs.
- Low calcination rate (1 °C/min) results in more ordered MBGs with higher surface area and pore volume compared to high calcination rate (20 °C/min).

Keywords Mesoporous bioactive glasses · Sol–gel · Calcination heating rate · Glass surface area · Glass pore volume

1 Introduction

Since their invention in the 1960s, bioactive glasses (BGs) have found increasing use in the clinical field. One of the main reasons for this is their ability to form an interfacial bond with host tissue [1]. This bond is formed as a result of the formation of a hydroxycarbonate apatite (HCA) layer, which is comparable in composition to the mineral phase of bone [2]. Bone cells will proliferate at the interface, causing bone growth into the BG [3]. Silica-based BGs have a network structure which can contain dopants to disrupt the continuity of the glass network, and form non-bridging silicon–oxygen bonds (Si-NBO) [4]. The number of Si-NBOs directly influences the bioactivity of the glasses, with a greater number of Si-NBO bonds leading to increased reactivity [4]. Dependent on dopants, they can also facilitate apatite deposition [5]. Gradual degradation and release of ionic species from the glass can have targeted effects such as inhibition of infection and angiogenesis [6].

Mesoporous materials were first synthesized in 1992 using surface-directing agents (surfactants) [7]. Mesoporous bioactive glasses (MBGs) possess channel structures resulting in high surface area (SA) [8]. This facilitates increased release of ions and results in improved bioactivity [9]. MBGs also possess higher pore volume (PV, ~0.45 cm^3/g) compared to BGs (~0.03 cm^3/g) [10] with pore sizes ranging from 2 to 50 nm [11]. These properties make MBG candidates for drug delivery [12], implant coatings [13], tissue engineering [13], bone grafting [14], dental [15], and hemostatic applications [16]. An ideal hemostat should have the following properties: it can achieve hemostasis within 2 min of application [17], it is biodegradable, anti-bacterial, suitable for both deep and irregular wounds, and non-inflammatory [18]. The porous morphology of MBGs can absorb water from the blood into their mesopores and can concentrate blood-clotting factors, accelerating hemostasis [19]. Their high surface area gives fast degradability and dopants can be used to inhibit bacterial infection and inflammation [20].

Sol–gels are stable suspensions of colloids in a porous gel network [21]. The sol–gel process is the building block for the synthesis of MBGs. There are two main parameters that affect the physical structure of MBGs (aside from composition): type of surfactant and calcination temperature. The effects of surfactant have been studied and reviewed, and the effects of surfactant on surface area, pore

volume, and pore size have been correlated [22]. CTAB (cetyltrimethylammonium bromide) produces the highest SA and PV, followed by the F-series poloxamers (F127 and F108), and lastly the P-series poloxamers (P123 and P85) [22]. The effect of calcination temperature was studied by Pereira et al. [23]. It was found that SA and PV decrease as the calcination temperature is increased from 400 to 800 °C. This was done without the use of surfactant [23]. The effect of calcination temperature, heating rate, and the residence time of thermal treatment for MBG scaffolds were studied by Shih et al. [24]. They synthesized MBG scaffolds utilizing F-127 as a surfactant at various calcination temperatures (400, 500, 600, 700, and 800 °C), using different heating rates (1, 10, and 20 °C/min) and with varying residence times (2, 4, 6, and 8 h). In their study, there was no clear correlation between the three parameters. To the authors' knowledge, the literature is lacking insight into the relationship between heating rate and MBGs' physical and chemical properties.

It is hypothesized that heating rate during calcination affects the physical and chemical structure of sol–gel glasses. In order to confirm this, two batches of MBG were synthesized using low (1 °C/min) and high (20 °C/min) heating rates. The physical structure and chemical composition of these two batches are compared and analyzed.

2 Synthesis and characterization

2.1 Materials

Reagent-grade triblock copolymer P123 ($EO_{20}PO_{70}EO_{20}$), calcium nitrate tetrahydrate [≥99.0%, $Ca(NO_3)_2.4H_2O$], triethyl phosphate (≥99.8%, TEP), tetraethyl orthosilicate (98%, TEOS), and ethanol (EtOH) were used. Reagent-grade hydrochloric acid (HCl) was diluted to 0.5 M HCl using deionized (DI) water. All reagents were purchased from Sigma Aldrich (Oakville, ON, Canada). For this work, P123 was chosen as a surface-directing agent because it yields more ordered mesoporous structures compared to other agents such as CTAB and F127 [22]. The more ordered channels facilitate better ion release compared to random channel structures.

2.2 Synthesis

MBG synthesis was performed following the process of Yan et al. [8]. Typically, 4 g of P123 and 1.4 g of calcium nitrate tetrahydrate were dissolved in 76 mL of EtOH. In a separate graduated cylinder, 1 mL of 0.5 M hydrochloric acid and 7.18 mL of TEOS were left to react for the acid-

Table 1 Compositions for synthesized MBGs (mol%)

Sample code	SiO_2	CaO	P_2O_5
H-MBG	80	15	5
L-MBG	80	15	5

catalyzed hydrolysis of TEOS. A volume of 0.68 mL TEP was added to the EtOH solution. Lastly, the TEOS-acid solution was poured into the EtOH solution. The solution was covered and stirred overnight. It was then transferred to a Petri dish for 5 days to allow for the evaporation-induced self-assembly (EISA) process. The EISA-derived gel was then calcined at 650 °C using a Hot Spot 110 furnace (Zircar Zirconia Inc., Florida, USA) for 6 h, with (20 and 1 °C/min) heating rates. The glasses have identical chemical compositions (Table 1).

The calcined samples were ground in a PM 100 ball mill (Retsch GmbH, Germany) at 500 revolutions per min (rpm) for 45 min. A 45-μm sieve was used to obtain powders with particle sizes <45 μm for characterization.

2.3 X-ray diffraction (XRD)

Small-angle X-ray diffraction (SAXRD) patterns were collected using an Anton Parr SAXS diffractometer (Anton Paar, Austria) with a Cu source from 0.2° to 10° (2θ), at a step size of 0.04°. A 2D detector was used with a photographic film and a 5-min exposure time for each sample. The operating voltage was 40 kV and the tube current was 50 mA.

Wide-angle X-ray diffraction (WAXRD) patterns were collected using a Philips PW3710 X-ray diffractometer (Phillips, Holland) with a Cu source from 10° to 80° (2θ), at a step size of 0.1° and count time of 2 s per step. A generator voltage of 45 kV and a tube current of 20 mA were employed.

2.4 Energy-dispersive X-ray spectroscopy (EDS) and X-ray photoelectron spectroscopy (XPS)

A JEOL 6380LV scanning electron microscope (JEOL, Massachusetts, USA) equipped with Oxford EDS was used to examine the chemical composition of each sample. The generating voltage used was 20 kV. A 1-cm Cu sample holder with double-sided carbon tape was pressed onto powder samples and placed into the scanning electron microscope (SEM) for analysis.

XPS was conducted on a K-Alpha XPS system (Thermo Fisher Scientific, Massachusetts, USA). Monochromated Al K-Alpha X-rays were used for analysis with a spot size of
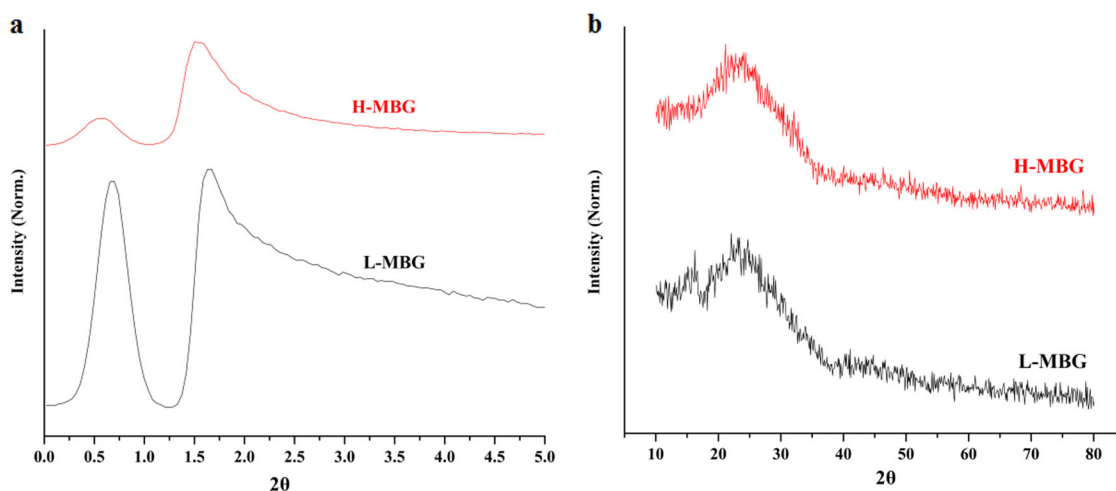
Fig. 1 Normalized **a** SAXRD and **b** WAXRD traces for H-MBG and L-MBG

400 μm. Charge compensation was achieved utilizing a low energy flood of electrons and ions at ~5×10^{-8} mbar vacuum. Residual pressure was from argon associated with operation of a charge compensation source. The survey spectrum was acquired in a high-pass energy (200 eV), low point-density (1 point/eV) scanned mode. Regional spectra used to determine the relative atomic composition, as well as for determination of chemical information, were acquired in a low-pass energy (50 eV), high point-density (0.1-eV spacing) scanned mode.

2.5 Fourier transform infrared (FTIR) spectroscopy

Attenuated total reflection Fourier transform infrared (ATR-FTIR) spectroscopy was carried out on the powder samples using an ATR-iS50 FTIR spectrometer (Thermo Scientific, Massachusetts, USA). Spectra were collected from 400 to 1500 cm^{-1} with a spectral resolution of 0.25 cm^{-1}.

2.6 Transmission electron microscopy (TEM)

Transmission electron microscopy was carried out on a Hitachi HT-7700 (Hitachi, Japan), using 80-kV generating voltage, to look at the structure of the nano-channels within the glass. Samples were embedded in modified Spurr's resin (Electron Microscopy Sciences, Pennsylvania, USA), ultramicrotomed, and then placed onto copper grids for imaging.

2.7 Brunauer–Emmett–Teller (BET) and Barrett–Joyner–Halenda (BJH) analysis

Surface area measurements were carried out by nitrogen gas adsorption in a Micromeritics Gemini VII 2390 gas

adsorption analyser (Micromeritics, Georgia, USA). The nitrogen (N_2) adsorption isotherm was measured at 77 K for both glasses. Surface area was then calculated using Brunauer–Emmett–Teller (BET) theory, and pore size distribution and pore volume were estimated using the Barrett–Joyner–Halenda (BJH) schema.

2.8 Ion release analysis

Ion release was conducted in DI water and analyzed using inductively coupled plasma-optical emission spectroscopy (ICP-OES). Fifty milligrams of sample was placed in a micro-centrifuge tube containing 1 mL of DI water. After the appropriate time intervals (15, 30, and 60 min), samples were centrifuged at 10,000 rpm for 2 min [25]. The supernatant was collected and diluted to conduct analyses.
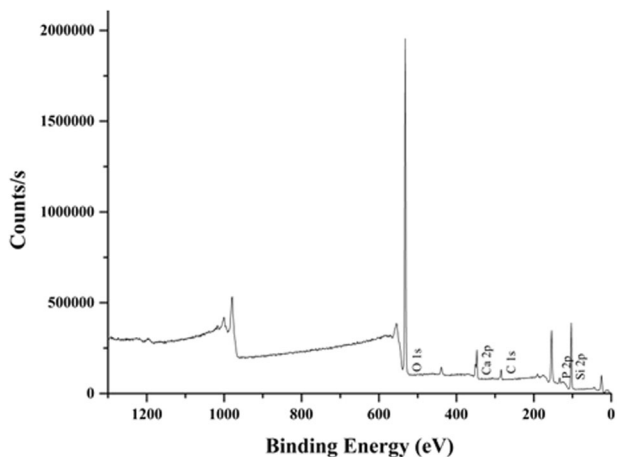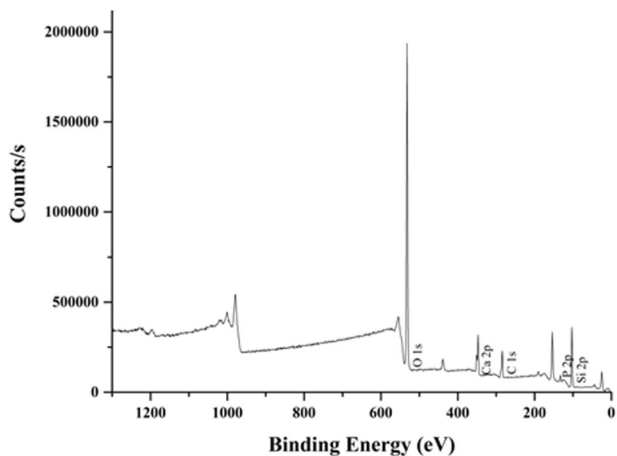
Chemical compositions of the collected samples were analyzed using ICP-OES, performed on an Optima 7300 DV ICP-OES (Perkin Elmer, Massachusetts, USA). Calibration standards for silicon, calcium, and phosphorus were prepared from a 1000 parts per million (ppm) stock solution. For the silicon sample, 1, 5, 10, and 25 ppm were used as calibration standards. For calcium, 0.5, 1, 5, and 10 ppm, and for phosphorus, 0.1, 0.5, 1, and 5 ppm calibration standards were used. In all cases, DI water was used as the blank.

2.9 Statistical analysis

Data were plotted using the mean ± standard deviation of samples ($n = 9$). Statistical analysis was performed using statistical package for social sciences (SPSS) software (IBM SPSS Statistics, version 24, New York, USA). Independent

Table 2 Summary of compositions (wt%) obtained from EDS

Sample	O	Si	Ca	P
L-MBG	58.60	31.40	7.23	2.77
H-MBG	63.36	27.30	7.17	2.17

Table 3 Normalized XPS data (at%)

Sample	O	Si	Ca	P
L-MBG	60.70	34.42	2.73	2.15
H-MBG	67.69	26.23	4.23	1.85

Fig. 2 XPS spectrum for L-MBG
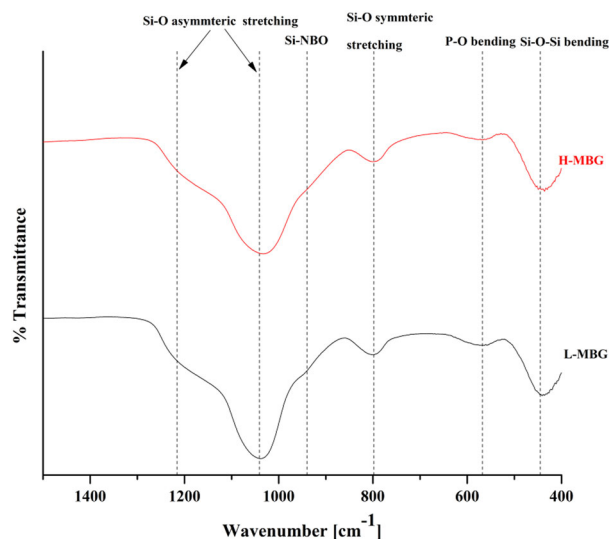
Fig. 4 FT-IR transmission spectra for L-MBG and H-MBG

Fig. 3 XPS spectrum for H-MBG

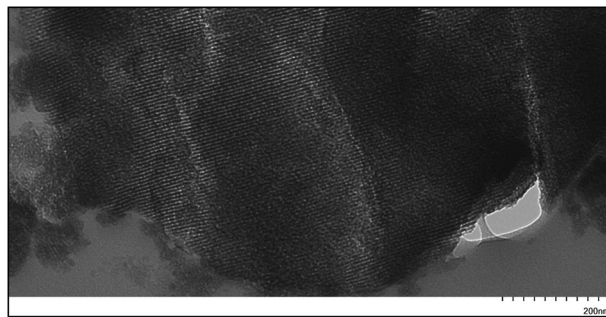**Fig. 5** TEM image of L-MBG at 30-k magnification

samples t test was used to analyze the data and to find out statistical significance with $p < 0.05$.

3 Results

Figure 1a shows the normalized SAXRD patterns for the H- and L-MBG samples. Both samples exhibited two diffraction peaks in the range 2θ from 0.2 to 2° which are characteristic of the P6mm space group [26] in hexagonal crystal systems. There is a slight right shift in the peak positions from H-MBG to L-MBG, and the intensity of the

H-MBG peaks is lower. Figure 1b shows the WAXRD patterns for both samples, confirming the amorphicity of both glasses.

EDS results (Table 2) confirm the presence of O, Si, Ca, and P in both glasses. Compositional data were also measured with XPS and relevant spectra for the glasses are shown in Figs. 2 and 3. Expected peaks for O, Si, Ca, and P are observed in the XPS spectrum. The carbon peak is due to the presence of adventitious carbon from adsorption of impurities during MBG handling and synthesis. Atomic percentages (normalized without carbon) are shown in Table 3 for L-MBG and H-MBG.

FTIR transmission spectra are shown in Fig. 4, along with the corresponding peaks. For L-MBG, the peak at 445
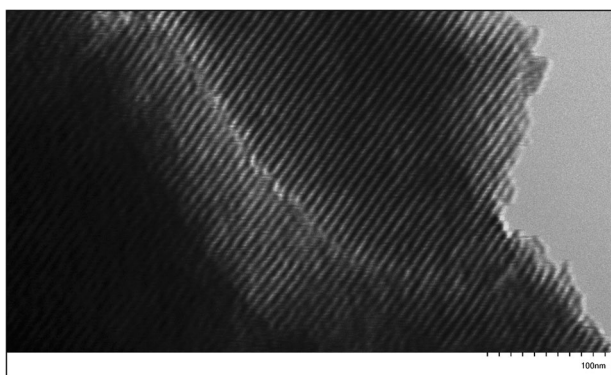
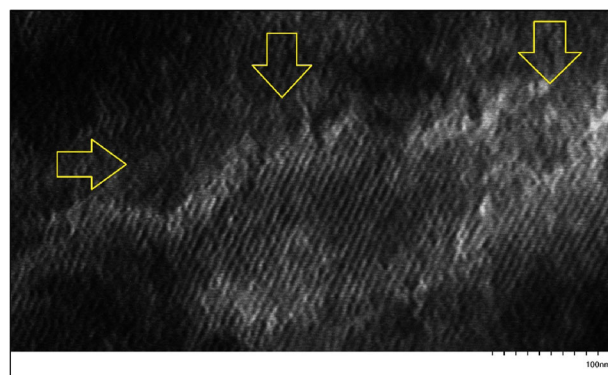Fig. 6 TEM image of L-MBG at 70-k magnification

Fig. 8 TEM image of H-MBG at 70-k magnification. Arrows indicate discontinuous regions of the mesoporous structure
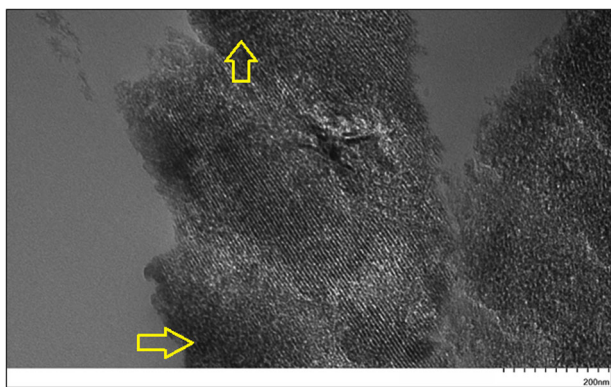

Fig. 7 TEM image of H-MBG at 30-k magnification. Arrow sign in the discontinuous regions of mesoporous channels

cm^{-1} represents Si–O–Si bending vibration [27], whereas the peak at 798 cm^{-1} indicates symmetric stretching of the Si–O bond [28]. The peak at 568 cm^{-1} corresponds to P–O bending mode [5]. Characteristic peaks located at 1041 and 1216 cm^{-1} are attributed to asymmetric stretching of Si–O bonds [29]. Lastly, the peak observed at 940 cm^{-1} is identified as the Si-NBO bond [29, 30]. In the case of H-MBG, all the functional groups were observed in the same intensities as L-MBG.

TEM images of L-MBG and H-MBG samples can be seen from Figs. 5 to 8, respectively. In the L-MBG sample, two-dimensional (2D) hexagonal well-ordered mesoporous channels are observed (Figs. 5 and 6). The TEM image of the H-MBG sample exhibits similar 2D hexagonal channels. However, H-MBG exhibits more discontinuities than L-MBG (Figs. 7 and 8).

Adsorption isotherms of both samples are shown in Fig. 9. They appear to be type IV isotherms in both cases, indicated by complete monolayer formation at low pressures, followed by capillary condensation at higher relative pressures (approaching relative saturation). This confirms a mesoporous-type surface structure in both cases—typical of adsorption curves for mesoporous glasses observed

elsewhere [31, 32]. BET surface area for L-MBG is 373.87 m^2/g and BJH adsorption cumulative pore volume is 0.27 cm^3/g. For H-MBG, BET surface area and BJH pore volume are 85.91 m^2/g and 0.13 cm^3/g, respectively. The average pore diameter is noted as 4.34 nm for L-MBG and 4.65 nm for H-MBG. Table 4 summarizes BET surface area, BJH pore volume, and average pore diameter results.

The ion release profiles for both sets of MBGs are shown in Fig. 10. It is observed that SiO_4^{4-} ion concentration increases significantly from 15 to 30 min, for L-MBG, and then begins to reach a steady state (Fig. 10a). The ions (SiO_4^{4-}, Ca^{2+}, and PO_4^{3-}) released from H-MBG have negligible change in concentration for consecutive time intervals (64.7, 56.3, and 54.8 ppm for SiO_4^{4-}; 21.1, 19, and 19.8 ppm for Ca^{2+}; and 5.6, 4.9, and 4.9 ppm for PO_4^{3-}).

4 Discussions

SAXRD peaks' presence indicates that both glasses have 2D hexagonal structure. Since the WAXRD shows that the glasses are amorphous, this structure is not from crystal formation but instead from the mesoporous architecture. The peaks are indicative of the P6mm space group in hexagonal lattice systems. Compositional data, measured through EDS and XPS, show that both L-MBG and H-MBG are chemically identical. Calcium content from the XPS data (Table 3) is lower than expected because XPS measures the surface composition more than the bulk. It has been shown that calcium ions remain in the bulk preferentially [33]. Analyzing FTIR transmission spectra (Fig. 4), there are no differences between the two samples' functional groups, meaning the two glasses are chemically identical.

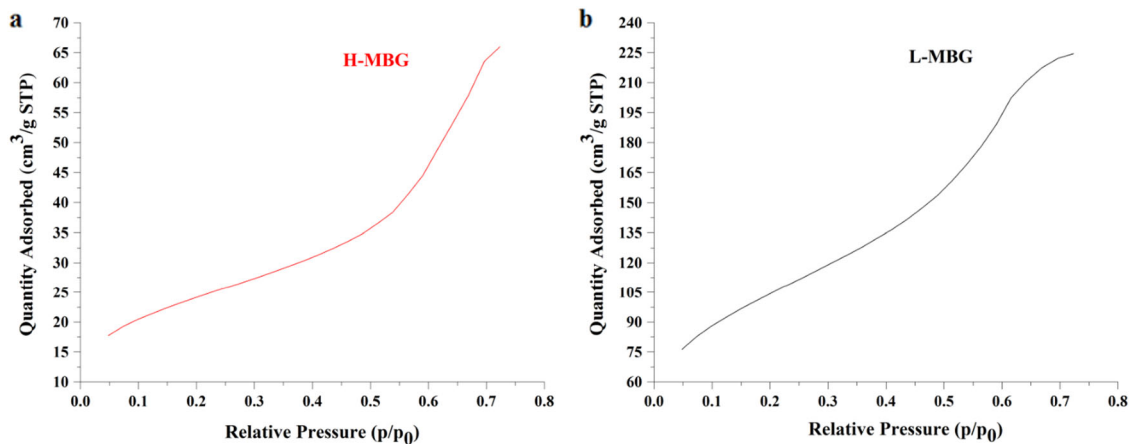TEM images (from Figs. 5 to 8) show that there are differences in the mesoporous architecture of the two

Fig. 9 Adsorption isotherm of **a** H-MBG and **b** L-MBG

Table 4 Physical properties of L-MBG and H-MBG

Sample	BET surface area (m^2/g)	BJH pore volume (cm^3/g)	BJH average pore diameter (nm)
L-MBG	373.87	0.27	4.34
H-MBG	85.91	0.13	4.65

glasses. The H-MBG has more discontinuities in the ordered channels (as seen in Figs. 7 and 8) compared to the L-MBG; this may be attributed to the higher heating rate. P123 is a hydrophilic surfactant and produces small, ordered micelles in aqueous media [21]. During the EISA process, the micelles self-assemble to create the mesoporous channels [34]. Calcination evaporates the micelles over time, leaving behind the mesoporous architecture. It is postulated that the rapid heating causes the micelles to evaporate vigorously out of the sample. Slow heating would result in the steady removal of the surfactant, retaining the integrity of the mesoporous structure (Figs. 5 and 6). The result of these discontinuities is the decrease in surface area and pore volume of the H-MBG samples. L-MBG exhibits more than fourfold higher surface area and twofold greater pore volume than H-MBG. Pore diameter data show that there is a minor increase (~7%) in pore diameter for H-MBG relative to L-MBG. This may be another effect of the vigorous evaporation caused by the high heating rate. Usually, the pore diameter is determined during the EISA process by the size of the micelles, not during calcination [21]. However, rapid heating can cause expansion of the micelles, thereby expanding the diameter of the channel. The increase in pore diameter is corroborated with SAXRD measurements. There is a slight right shift of the peaks from the H-MBG to the L-MBG samples. This can be attributed

to a decrease in pore diameter from H-MBG to L-MBG, as smaller spacings diffract at higher angles. H-MBG also has a lower peak intensity because the discontinuities in the structure do not allow for constructive interference of the diffracted X-rays. Higher peak intensity reflects the higher ordered structure of L-MBG [35].

The change in surface area directly affects the ion release of the samples. SiO_4^{4-} ion release from H-MBG is significantly lower compared to L-MBG (Fig. 10a). This is due to L-MBG having higher surface area and a more ordered channel structure compared to H-MBG, resulting in its faster degradation. It is also noted that Ca^{2+} and PO_4^{3-} ion concentration of L-MBG samples decreased after 30 min (Fig. 10b, c). A possible explanation for this is the development of some calcium phosphate on the glass surface. This would cause a depletion in the solution Ca^{2+} and PO_4^{3-} concentrations, and so explains why the concentration decreased for both ions. Lower concentration of ions from H-MBG is the result of low surface area and pore volume causing slower degradation of the H-MBG. There is a statistically significant ($p < 0.05$) increase of ions from L-MBG after 15, 30, and 60 min relative to H-MBG. These time intervals were chosen based on the proposed use of these MBGs as hemostats for short-term blood coagulation (persistence of bleeding for long durations requires surgical closing). Platelet plug formation in primary hemostasis occurs within an hour [36]. The mechanism by which MBGs achieve hemostasis is thought to be a physical process (absorption of water and concentration of clotting factors). For this, high surface area and pore volume are more critical compared to the concentration of ions released. Since Ca^{2+} ions speed up the coagulation process, any increase in the concentration of this ion is beneficial [37]. Since L-MBGs provide a greater increase in the Ca^{2+} ion, their effect on hemostasis will also be greater.
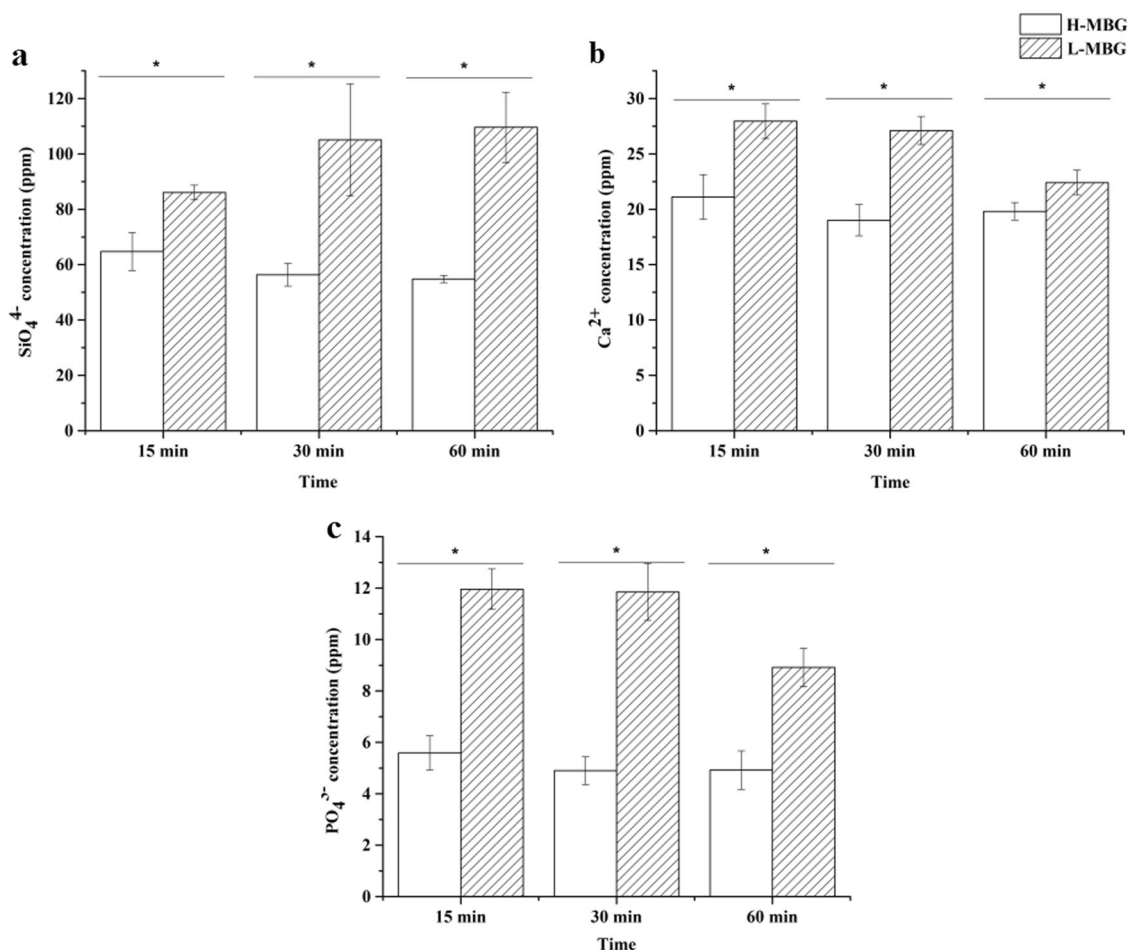
Fig. 10 **a** SiO_4^{4-}, **b** Ca^{2+}, and **c** PO_4^{3-} ion release from L-MBG and H-MBG samples. Error bar represents standard deviation from the mean ($n = 9$). * Represents statistical significance between samples ($p < 0.05$)

5 Conclusions

Two batches of mesoporous bioactive glass were formulated from identical starting reagents, and the effect of calcination rate on composition and structure was evaluated. WAXRD, EDS, XPS, and FTIR results confirmed that heating rate does not influence chemical composition.

Analyzing TEM, BET, and SAXRD results, it is evident that the calcining rate does influence the physical structure of the MBGs. TEM imaging gave a visual of many discontinuities in the mesoporous channels for H-MBG, and BET quantified its low specific surface area and pore volume, and higher pore diameter. Relatively, L-MBGs had few discontinuities, a fourfold greater specific surface area, and a twofold greater pore volume. This led to larger amounts of ions released from L-MBG compared to H-MBG.

L-MBGs have high potential as hemostats because the greater surface area allows for more water absorption/clotting factor concentration, and releases more Ca^{2+} for speeding up hemostasis.

The results presented in this study provide insight on the effects of heating rate on the physical structure of MBGs. During synthesis, low heating rate is best for getting well-structured mesoporous channels.

5.1 Limitations

Calcination heating rate was only varied once: 1 and 20 °C/min. More heating rates could be tested intermittently to find an ideal heating rate for faster experimental time but few MBG discontinuities.

This study does not include in vitro or in vivo data to explain the effect of changing the heating rate on the in vitro apatite formation or cell activity, however, this will be the focus of a follow-up manuscript.

Compliance with ethical standards

References

1. Ylänen HO (2011) Bioactive glasses materials, properties and applications, 1st edn. Woodhead Publishing Limited, Cambridge, United Kingdom
2. Farooq I, Imran Z, Farooq U, Leghari A, Ali H (2012) Bioactive glass: a material for the future. World J Dent 3:199–201. https://doi.org/10.5005/jp-journals-10015-1156
3. Hench LL (2013) An introduction to bioceramics. 2nd ed., Imperial College Press, Singapore
4. González P, Serra J, Liste S, Chiussi S, León B, Pérez-Amor M (2003) Raman spectroscopic study of bioactive silica based glasses J Non Cryst Solids 320:92–99. https://doi.org/10.1016/S0022-3093(03)00013-9
5. O'Donnell MD, Watts SJ, Hill RG, Law RV (2009) The effect of phosphate content on the bioactivity of soda-lime- phosphosilicate glasses. J Mater Sci Mater Med 20:1611–1618. https://doi.org/10.1007/s10856-009-3732-2
6. Mohamed APT, Rahaman N, Day DE, Bal BS, Fu Q, Jung SB, Bonewald LyndaF (2013) Bioactive glass in tissue engineering. J Mater Sci Mater Med 24:669–676. https://doi.org/10.1016/j.actbio.2011.03.016.Bioactive
7. Kresge CT, Leonowicz ME, Roth WJ, Vartuli JC, Beck JS (1992) Ordered mesoporous molecular sieves synthesized by a liquid-crystal template mechanism. Nature 359:710–712. https://doi.org/10.1038/359710a0
8. Yan X, Yu C, Zhou X, Tang J, Zhao D (2004) Highly ordered mesoporous bioactive glasses with superior in vitro bone-forming bioactivities. Angew Chem Int Ed 43:5980–5984. https://doi.org/10.1002/anie.200460598
9. Wu C, Chang J (2014) Multifunctional mesoporous bioactive glasses for effective delivery of therapeutic ions and drug/growth factors. J Control Release 193:282–295. https://doi.org/10.1016/j.jconrel.2014.04.026
10. Sepulveda P, Jones JR & Hench LL (2001) Characterization of melt-derived 45S5 and sol-gel-derived 58S bioactive glasses, J Biomed Mater Res 734–740. https://doi.org/10.1002/jbm.0000
11. S T, Sing KSW, Everett DH, Haul RAW, Moscou L, Pierotti RA, Rouquerol J (1985) IUPAC. Gas/solid systems with special reference to the determination of surface area and porosity. Pure Appl Chem 57:603–619. https://doi.org/10.1351/pac198557040603
12. Li Y, Liu YZ, Long T, Bin X, Tang Yu TT, Dai KR, Tian B, Guo YP, Zhu ZA (2013) Mesoporous bioactive glass as a drug delivery system: Fabrication, bactericidal properties and biocompatibility J Mater Sci Mater Med 24:1951–1961. https://doi.org/10.1007/s10856-013-4960-z
13. Ye J, He J, Wang C, Yao K, Gou Z (2014) Copper-containing mesoporous bioactive glass coatings on orbital implants for improving drug delivery capacity and antibacterial activity. Biotechnol Lett 36:961–968. https://doi.org/10.1007/s10529-014-1465-x
14. Alcaide M, Portolés P, López-Noriega A, Arcos D, Vallet-Regí M, Portolés MT (2010) Interaction of an ordered mesoporous bioactive glass with osteoblasts, fibroblasts and lymphocytes, demonstrating its biocompatibility as a potential bone graft material. Acta Biomater 6:892–899. https://doi.org/10.1016/j.actbio.2009.09.008
15. Zhang Y, Chen L, Shi M, Zhai D, Zhu H, Chang J, Wu C, Zheng X, Yin J (2016) Mesoporous bioactive glass nanolayer-modified zirconia coatings on Ti-6Al-4V with improved in vitro bioactivity. Int J Appl Glas Sci 7:216–228. https://doi.org/10.1111/ijag.12210
16. Vichery C, Nedelec J-M (2016) Bioactive glass nanoparticles: from synthesis to materials design for biomedical applications. Materials 9:288. https://doi.org/10.3390/ma9040288
17. Khoshmohabat H, Paydar S, Kazemi HM, Dalfardi B (2016) Overview of agents used for emergency hemostasis. Trauma Mon 21. https://doi.org/10.5812/traumamon.26023
18. Kheirabadi B Evaluation of topical hemostatic agents for combat wound treatment (2011) US Army Med Dep J, 25–37
19. Hu G, Xiao L, Tong P, Bi D, Wang H, Ma H, Zhu G, Liu H (2012) Antibacterial hemostatic dressings with nanoporous bioglass containing silver. Int J Nanomed 7:2613–2620. https://doi.org/10.2147/IJN.S31081
20. Pourshahrestani S, Zeimaran E, Adib Kadri N, Gargiulo N, Samuel S, Naveen SV, Kamarul T, Towler MR (2016) Gallium-containing mesoporous bioactive glass with potent hemostatic activity and antibacterial efficacy. J Mater Chem B 4:71–86. https://doi.org/10.1039/C5TB02062J
21. David Levy MZ (2015) The sol-gel handbook. 1st edn Wiley-VCH Verlag GmbH & Co. KGaA, Boschstr., 10.1002/9783527670819
22. Wu C, Chang J (2012) Mesoporous bioactive glasses: structure characteristics, drug/growth factor delivery and bone regeneration application. Interface Focus 2:292–306. https://doi.org/10.1098/rsfs.2011.0121
23. Pereira MM, Clark AE, Hench LL (1995) Effect of texture on the rate of hydroxyapatite formation on gel-silica surface. J Am Ceram Soc 78:2463–2468. https://doi.org/10.1111/j.1151-2916.1995.tb08686.x
24. Shih CJ, Chen HT, Huang LF, Lu PS, Chang HF, Chang IL (2010) Synthesis and in vitro bioactivity of mesoporous bioactive glass scaffolds. Mater Sci Eng C 30:657–663. https://doi.org/10.1016/j.msec.2010.02.006
25. Majekodunmi SO (2015) A review on centrifugation in the pharmaceutical industry. Am J Biomed Eng 5:67–78. https://doi.org/10.5923/j.ajbe.20150502.03
26. van Steen E, Claeys M, Callanan LH (2004) Recent advances in the science and technology of zeolites and related materials 880, 154, Elsevier, Cape Town, South Africa
27. El-Kady AM, Ali AF (2012) Fabrication and characterization of ZnO modified bioactive glass nanoparticles. Ceram Int 38:1195–1204. https://doi.org/10.1016/j.ceramint.2011.07.069
28. Philippart A, Boccardi E, Pontiroli L, Beltrán AM, Inayat A, Vitale-Brovarone C, Schwieger W, Spiecker E, Boccaccini AR (2014) Development of novel mesoporous silica-based bioactive glass scaffolds with drug delivery capabilities. Adv Sci Technol 96:54–60. https://doi.org/10.4028/www.scientific.net/AST.96.54

29. Serra J, González P, Liste S, Serra C, Chiussi S, León B, Pérez-Amor M, Ylänen HO, Hupa M (2003) FTIR and XPS studies of bioactive silica based glasses. J Non Cryst Solids 332:20–27. https://doi.org/10.1016/j.jnoncrysol.2003.09.013

30. Shah AT, Ain Q, Chaudhry AA, Khan AF, Iqbal B, Ahmad S, Siddiqi SA, ur Rehman I (2015) A study of the effect of precursors on physical and biological properties of mesoporous bioactive glass. J Mater Sci 50:1794–1804. https://doi.org/10.1007/s10853-014-8742-x

31. Lu W, Li K, Lu C, Teoh L (2013) Synthesis and characterization of mesoporous SiO 2–CaO–P 2 O 5 bioactive glass by sol–gel process. Mater Trans 54:791–795. https://doi.org/10.2320/matertrans.M2012417

32. Sanchez-Salcedo S, Malavasi G, Salinas AJ, Lusvardi G, Rigamonti L, Menabue L, Vallet-Regi M (2018) Highly-bioreactive silica-based mesoporous bioactive glasses enriched with gallium (III). Materials 11:1–17. https://doi.org/10.3390/ma11030367

33. Perez-Pariente J, Balas F, Vallet-Regi M (2000) Surface and chemical study of SiO2·P2O5·CaO·(MgO) bioactive glasses. Chem Mater 12:750–755. https://doi.org/10.1021/cm9911114

34. A.S., H.F. C, Brinker Jeffrey, Lu Yunfeng (1999) Evaporation-induced self-assembly: nanostructures made easy. Adv Mater 11:579–585

35. Zhao D, Wan Y, Zhou W (2013) Ordered mesoporous materials, Wiley-VCH Verlag GmbH & Co. KGaA https://doi.org/10.1002/9783527647866.

36. Boon GD (1993) An overview of hemostasis. Toxicol Pathol 21:170–179. https://doi.org/10.1177/019262339302100209

37. Smit Sibinga C, Das PC & Mannucci PM (1992) Coagulation and blood transfusion https://doi.org/10.1097/00001721-199206000-00015.